

Fast degradation of the circular flare ribbon on 2014 August 24

Q. M. Zhang^{1,2}, S. H. Yang^{2,3}, T. Li^{2,3}, Y. J. Hou^{2,3}, and Y. Li¹

¹ Key Laboratory of Dark Matter and Space Science, Purple Mountain Observatory, CAS, Nanjing 210033, PR China
e-mail: zhangqm@pmo.ac.cn

² CAS Key Laboratory of Solar Activity, National Astronomical Observatories, Chinese Academy of Sciences, Beijing 100101, PR China

³ School of Astronomy and Space Science, University of Chinese Academy of Sciences, Beijing 100049, PR China

Received; accepted

ABSTRACT

Context. The separation and elongation motions of solar flare ribbons have extensively been investigated. The degradation and disappearance of ribbons have rarely been explored.

Aims. In this paper, we report our multiwavelength observations of a C5.5 circular-ribbon flare associated with two jets (jet1 and jet2) on 2014 August 24, focusing on the fast degradation of the outer circular ribbon (CR).

Methods. The flare was observed in ultraviolet (UV) and extreme-ultraviolet (EUV) wavelengths by the Atmospheric Imaging Assembly (AIA) on board the Solar Dynamics Observatory (SDO) spacecraft. Soft X-ray (SXR) fluxes of the flare in 0.5–4 and 1–8 Å were recorded by the GOES spacecraft.

Results. The flare, consisting of a short inner ribbon (IR) and outer CR, was triggered by the eruption of a minifilament. The brightness of IR and outer CR reached their maxima simultaneously at ~04:58 UT in all AIA wavelengths. Subsequently, the short eastern part of CR faded out quickly in 1600 Å but gradually in EUV wavelengths. The long western part of CR degraded in the counterclockwise direction and experienced a deceleration. The degradation was distinctly divided into two phases: phase I with faster apparent speeds (58–69 km s⁻¹) and phase II with slower apparent speeds (29–35 km s⁻¹). The second phase stopped at ~05:10 UT when the western CR totally disappeared. Besides the outward propagation of jet1, the jet spire experienced untwisting motion in the counterclockwise direction during 04:55–05:00 UT.

Conclusions. We conclude that the event can be explained by the breakout jet model. The coherent brightenings of the IR and CR at ~04:58 UT may result from the impulsive interchange reconnection near the null point, whereas sub-Alfvénic slipping motion of the western CR in the counterclockwise direction indicates the occurrence of slipping magnetic reconnection. Another possible explanation of the quick disappearance of the hot loops connecting to the western CR is that they are simply reconnected sequentially without the need for significant slippage after the null point reconnection.

Key words. Sun: magnetic fields – Sun: flares – Sun: filaments, prominences – Sun: UV radiation – Sun: X-rays, gamma rays

1. Introduction

Solar flares are one of the most powerful activities in the solar atmosphere (Fletcher et al. 2011). Amount to 10²⁹–10³² erg magnetic free energy is impulsively released via magnetic reconnection within tens of minutes to a few hours (Emslie et al. 2012; Yang et al. 2015; Li et al. 2017a; Chen et al. 2019b; Hong et al. 2019; Zhang et al. 2019b). In the context of collisional thick-target flare model, high-energy electrons stream downward into the cool and dense chromosphere where electrons are stopped by Coulomb collisions and lose energy, heating the localized plasma to ~10⁷ K and driving chromospheric evaporation (Brown 1971; Fisher et al. 1985). Emissions at the flare ribbons or kernels increase dramatically in optical, ultraviolet (UV), extreme-ultraviolet (EUV), hard X-ray (HXR), and microwave wavelengths (e.g., Krucker et al. 2011; Fletcher et al. 2013; Sharykin & Kosovichev 2014; Jing et al. 2016; Chen et al. 2019a). After reaching the peak value, the brightness of ribbons begins to decrease as a result of conductive and radiative cooling (Cargill et al. 1995).

As magnetic reconnection in the corona proceeds, the double flare ribbons separate with time (Qiu et al. 2002, 2004). The rate

of reconnection could be estimated based on the separation speed (20–100 km s⁻¹) and line-of-sight (LOS) magnetic field strength on the conjugate ribbons. High-cadence and high-resolution observations reveal that the distance between the double centroids of H α bright kernels decreases at the rising phase of the HXR spikes and increases after the flare peak time (Ji et al. 2004, 2006). Apart from the separation, the brightening may propagate along the flare ribbons at speeds of a few to 100 km s⁻¹ (Qiu 2009; Qiu et al. 2017). During three-dimensional (3D) magnetic reconnection within the thin quasi-separatrix layer (QSL; Demoulin et al. 1996) where the gradient in field-line linkage is sharp and electric current accumulates, the flare ribbons propagate along the intersection of QSL with the photosphere (e.g., Aulanier et al. 2007; Janvier et al. 2013; Li & Zhang 2015; Janvier et al. 2016; Savcheva et al. 2016; Zhao et al. 2016).

Circular-ribbon flares (CRFs) are a special kind of flares whose ribbons have circular or quasi-circular shapes (e.g., Masson et al. 2009; Wang & Liu 2012; Hernandez-Perez et al. 2017; Li et al. 2018; Chen et al. 2019a; Hou et al. 2019). In most cases, they are triggered by filament eruptions (Yang & Zhang 2018; Li & Yang 2019). The 3D magnetic configuration asso-

Table 1. Description of the observational parameters.

Instrument	λ (Å)	Time (UT)	Cad. (s)	Pix. Size (")
SDO/AIA	94–335	04:30–06:00	12	0.6
SDO/AIA	1600	04:30–06:00	24	0.6
GOES	0.5–4.0	04:30–06:00	2.05	...
GOES	1–8	04:30–06:00	2.05	...

ciated with a CRF usually features a magnetic null point and the corresponding fan-spine skeleton (Xu et al. 2017; Li & Yang 2019). The inner ribbon (IR) is shorter and brighter than the outer circular ribbon (CR), implying that the energy deposition is more concentrated in the inner ribbon (Zhang et al. 2016a,b). The chromospheric brightening of a CRF is not always simultaneous but sequential, with apparent speeds of ten to 220 km s⁻¹ (Wang & Liu 2012; Li et al. 2017b; Romano et al. 2017; Xu et al. 2017; Li et al. 2018). So far, the degradation and disappearance of flare ribbons have rarely been investigated.

In this paper, we report our multiwavelength observations of the C5.5 CRF on 2014 August 24, focusing on the fast degradation of the outer CR. In Sect. 2, we describe the data analysis. Results are presented in Sect. 3. We compare our findings with previous models and give a brief summary in Sect. 4.

2. Observations and data analysis

The C5.5 flare in NOAA active region (AR) 12149 (N10E44) was observed by the Atmospheric Imaging Assembly (AIA; Lemen et al. 2012) on board the Solar Dynamics Observatory (SDO). AIA takes full-disk images in two UV (1600 and 1700 Å) and seven EUV (94, 131, 171, 193, 211, 304, and 335 Å) wavelengths. The level_1 data were calibrated using the standard solar software program `aia_prep.pro`. Soft X-ray (SXR) light curves of the flare in 0.5–4 and 1–8 Å were recorded by the GOES spacecraft. The observational parameters are listed in Table 1.

3. Results

In Fig. 1, the bottom panel shows the SXR light curves of the flare. It is clear that the SXR emissions started to rise at ~04:55 UT and reached the peak values at ~05:02 UT, which were followed by a gradual decay phase until ~05:25 UT. Since the HXR flux during the flare was not available, we take time derivative of the 1–8 Å flux as a HXR proxy according to the Neupert effect. In Fig. 1(a), two spikes at 04:58:36 UT and 04:59:18 UT are remarkable, which are concurrent with the primary and second peaks in 1600 Å (see Fig. 1(d) in Zhang et al. (2019a)). A plausible reason for these spikes is intermittent magnetic reconnection and subsequent energy input in the chromosphere by nonthermal electrons (Zhang et al. 2016b).

In Fig. 2, eight snapshots of the AIA 304 Å images illustrate the evolution of flare (see also the online animation *anim304.mov*). Before the flare, there were three minifilaments (F1, F2, and F3) at the flaring region. Impulsive eruption of the eastern filament (F1) resulted in strong heating of the filament and generation of the first blowout jet (jet1) (see panels (b)–(c)). Meanwhile, magnetic reconnection at the null point may be triggered (Priest & Pontin 2009; Zhang et al. 2012; Baumann et al. 2013). The accelerated nonthermal electrons propagate downward along the fan-spine field lines and precipitate in the chro-

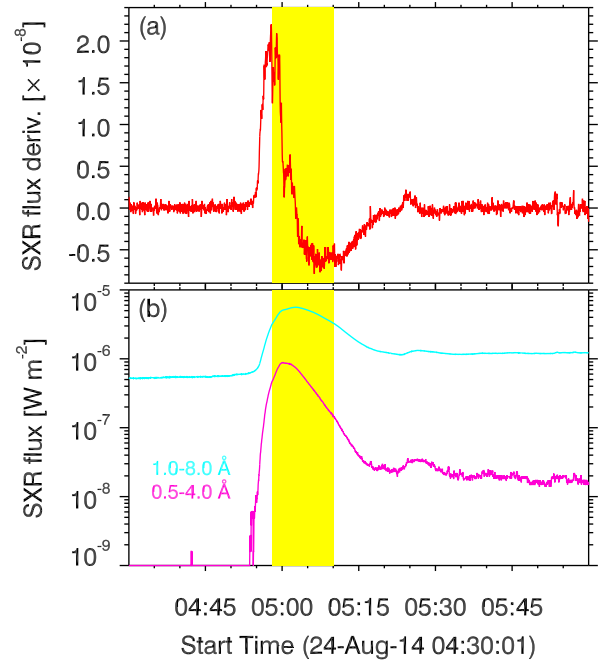


Fig. 1. Bottom panel: SXR light curves of the C5.5 flare in 0.5–4 Å (magenta line) and 1–8 Å (cyan line). Top panel: Time derivative of the 1–8 Å flux. In each panel, the yellow region stands for the time of fast degradation of the outer circular ribbon.

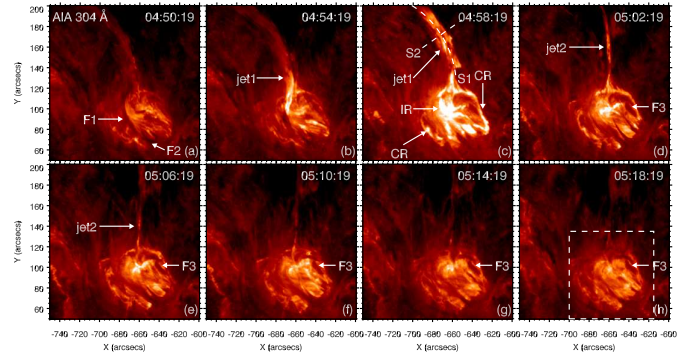


Fig. 2. Eight snapshots of the AIA 304 Å images during 04:50–05:18 UT. The white arrows point to the circular ribbon (CR), inner ribbon (IR), two jets (jet1, jet2), and three filaments (F1, F2, F3). Two slices (S1 and S2) in panel (c) are used for investigating the propagation and rotation of jet1, respectively. The white dashed box in panel (h) signifies the field of view of Fig. 3. Evolution of the flare is shown in a movie (*anim304.mov*) available online.

mosphere. The impulsive heating results in the CRF, which consists of a compact IR and the surrounding CR. The brightness of IR and CR reached their maxima at ~04:58 UT. Shortly afterwards, another jet (jet2) appeared adjacent to jet1 and propagated northward (see panel (d)). Subarcsecond blobs (plasmoids) with an average size of 0''.78 were detected in the jets (Zhang & Ni 2019). The southern minifilament (F2) and western minifilament (F3) were undisturbed and remained there (see panels (d)–(h)).

In Fig. 3, the left column (a1–a6) shows the evolution of flare ribbons in 94 Å ($\log T \approx 6.8$). It is seen that bright post-flare loop (PFL) became evident as magnetic reconnection proceeded. During 04:58–05:04 UT, converging motion of hot plasma along the PFL towards the loop top was detected, which is a clear indication of chromospheric evaporation (Zhang et al. 2019a). The

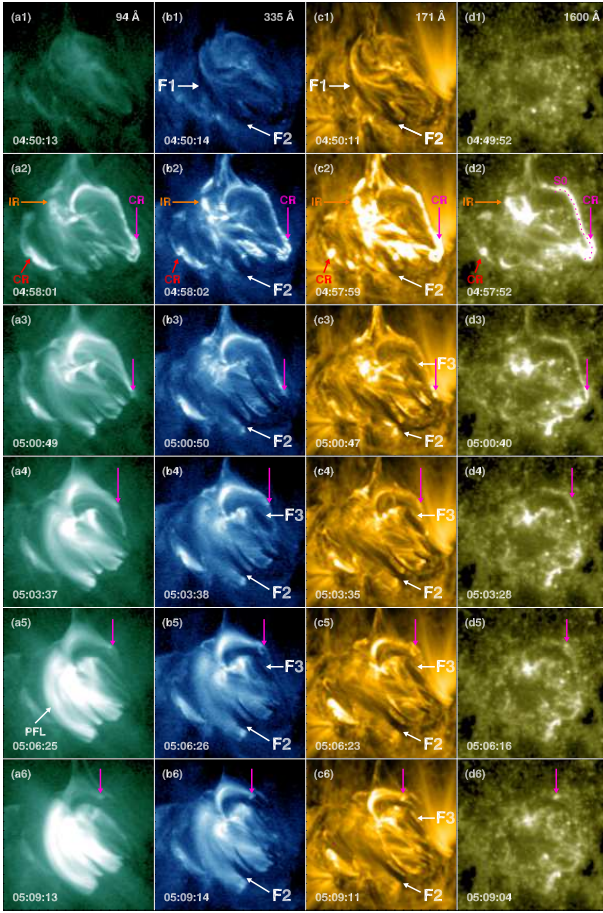


Fig. 3. Evolution of the flare ribbons observed in AIA 94 Å (a1-a6), 335 Å (b1-b6), 171 Å (c1-c6), and 1600 Å (d1-d6). The white arrows point to F1, F2, F3, and PFL. The orange arrows point to the IR. The red and magenta arrows point to the eastern and western parts of CR, respectively. Evolution of the CR is shown in a movie (*animrb.mov*) available online.

second, third, and fourth columns of Fig. 3 show the evolution of ribbons in 335 Å ($\log T \approx 6.4$), 171 Å ($\log T \approx 5.8$), and 1600 Å, respectively. As mentioned above, the brightness of IR and outer CR reached their maxima simultaneously at $\sim 04:58$ UT in all AIA wavelengths, which is consistent with the HXR peak time (see Fig. 1(a)). Subsequently, the short eastern part of CR, which is pointed by the red arrows, faded out quickly in 1600 Å (see panels (d2)–(d6)) but gradually in EUV wavelengths. The long western part of CR, which is pointed by the magenta arrows, did not fade out coherently as expected. Instead, the CR degraded in the counterclockwise direction during 04:58–05:10 UT.

In Fig. 3(d2), a curved artificial slice (S0) along the western CR is selected. The time-distance diagrams of S0 in various wavelengths are displayed in Fig. 4. It is obvious that the CR brightened simultaneously at $\sim 04:58$ UT in all wavelengths. Then, the CR degraded counterclockwise and experienced a deceleration. The degradation was obviously divided into two phases: phase I with faster apparent speeds (58 – 69 km s $^{-1}$) and phase II with slower apparent speeds (29 – 35 km s $^{-1}$). The average speed of phase I is ~ 2.1 times higher than that of phase II. The second phase stopped at $\sim 05:10$ UT when the western CR totally disappeared.

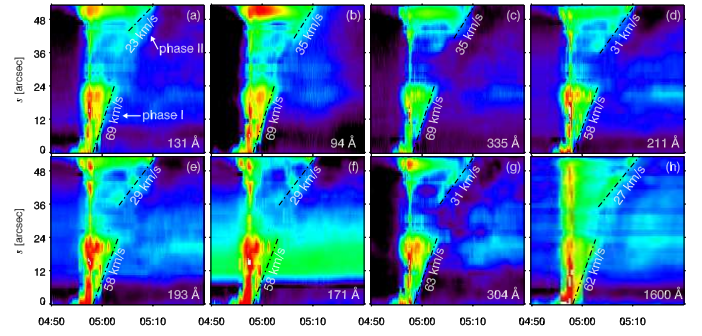


Fig. 4. Time-distance diagrams of S0 in various wavelengths, showing the fast degradation of the western CR during 04:58–05:10 UT. The apparent speeds are labeled. $s = 0$ and $s = 52''8$ on the y -axis denote the southern and northern endpoints of S0, respectively.

Table 2. Apparent speeds (km s $^{-1}$) of degradation of the western CR in different AIA wavelengths (Å).

λ	131	94	335	211	193	171	304	1600
ph_I	69	69	69	58	58	58	63	62
ph_II	23	35	35	31	29	29	31	27

4. Discussion and summary

To explain how accelerated particles at a reconnection site could finally propagate along the Earth-connected open flux tube, Masson et al. (2012) performed a 3D numerical simulation under the magnetic topology of an asymmetric coronal null point, with a closed fan surface and an open outer spine. It is found that interchange magnetic reconnection takes place when field lines anchored below the fan dome reconnect at the null point and jump to the open magnetic domain. The reconnected field lines near the outer spine keep reconnecting continuously and show apparent slipping motion, which is quite different from the case in 2D. Recently, Wyper et al. (2018) performed 3D numerical simulations of coronal jets with filaments, confirming the breakout jet generation mechanism (Wyper et al. 2017). The untwisting, blowout jets are produced by a combination of an untwisting flux rope and plasma accelerated by the flare reconnection below. Doyle et al. (2019) studied a helical jet associated with a C1.5 flare triggered by a confined filament eruption on 2013 June 30. The erupting filament material was partially transferred into the outflow jet along large-scale, overlying coronal loops. Additionally, the authors conducted a 3D MHD numerical simulation of a breakout jet in a closed-field configuration and found excellent qualitative agreement with observations. Hence, it is concluded that the confined eruption with a rotating jet could well be explained by the breakout model (Wyper et al. 2017, 2018).

In our study, the first jet (jet1) associated with the C5.5 CRF also shows untwisting motion. In Fig. 2(c), two artificial slices (S1 and S2) along and across the jet spire are selected. The time-distance diagrams of S1 and S2 in 304 Å are displayed in the left and right panels of Fig. 5, respectively. The apparent propagation speed of jet1 during 04:55–05:00 UT is calculated to be ~ 300 km s $^{-1}$. In panel (b), it is obvious that the jet spire shows untwisting motion in the counterclockwise direction when looking down and splits into two threads during 04:55–05:00 UT. The apparent speeds of untwisting motion are estimated to be ~ 59 and ~ 63 km s $^{-1}$. It is noted that jet2 does not show significant rotation, possibly due to that the twist (helicity) in the erupting filament (F1) has entirely been transported to the large-scale

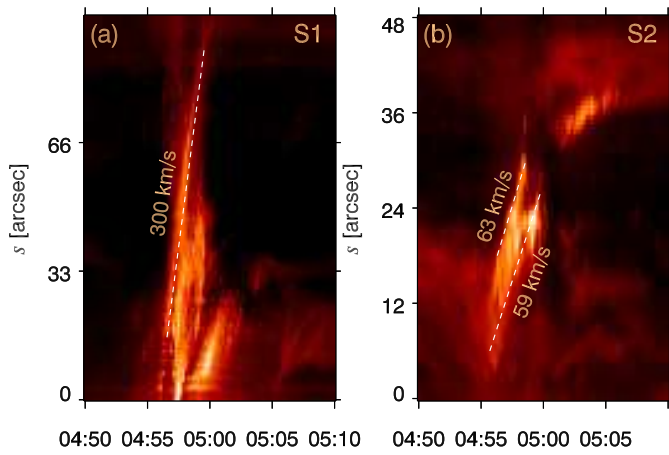


Fig. 5. Time-distance diagrams of S1 and S2 in 304 Å. The apparent speeds are labeled. In panel (a), $s = 0$ and $s = 99''$ on the y -axis denote the southern and northern endpoints of S1. In panel (b), $s = 0$ and $s = 48''$ on the y -axis denote the eastern and western endpoints of S2.

coronal loops during jet1. Therefore, the CRF associated with an untwisting jet triggered by the eruption of a minifilament can be interpreted by the breakout model (Wyper et al. 2018). The coherent brightenings of the IR and CR at $\sim 04:58$ UT may result from the impulsive interchange reconnection near the null point, whereas sub-Alfvénic slipping motion of the western CR in the counterclockwise direction is indicative of slipping magnetic reconnection. The apparent speeds of degradation are close to the speeds of elongation of the CR during the second episode in the event of Li et al. (2018). The deceleration of degradation from phase I to phase II suggests that magnetic reconnection tapered off.

It is revealed in the breakout jet model that the magnetic flux of strapping field overlying the erupting filament is transferred to the other side of the fan dome, allowing the filament to reach the null point, where it is reconnected and produces a helical jet. Meanwhile, a flare current sheet is formed beneath the filament, so that the reconnected overlying flux is reconnected back to where the filament originated. In Fig. 3(a3), hot newly reconnected loops appeared, connecting to the western CR. Those hot loops might be the breakout loops on the other side of F1 (see also Fig. 9(b) in Doyle et al. (2019)). The sequential disappearance of those hot loops during 04:58–05:04 UT is not only concurrent with the fast degradation of western CR in phase I, but also consistent with the brightening of PFL to the east side of anemone (see Fig. 3(a4–a6)). The evolution is evidently illustrated in Fig. 9 of Doyle et al. (2019) and is nicely in agreement with the breakout jet model by Wyper et al. (2018). Therefore, another possible explanation of the quick disappearance of the hot loops connecting to the western CR is that they are simply reconnected sequentially without the need for significant slipping after the null point reconnection.

In this work, we report our multiwavelength observations of a C5.5 CRF associated with two jets on 2014 August 24. The flare, consisting of a short IR and outer CR, was triggered by the eruption of a minifilament. The brightness of IR and CR reached their maxima simultaneously at $\sim 04:58$ UT in all AIA wavelengths. Afterwards, the short eastern part of CR faded out quickly in 1600 Å but gradually in EUV wavelengths. The long western part of CR degraded in the counterclockwise direction and experienced a deceleration. The degradation was distinctly divided into two phases: phase I with faster apparent speeds

(58–69 km s^{−1}) and phase II with slower apparent speeds (29–35 km s^{−1}). The second phase stopped at $\sim 05:10$ UT when the western CR completely disappeared. Apart from the longitudinal propagation of jet1, the jet spire experienced untwisting motion in the counterclockwise direction during 04:55–05:00 UT. We conclude that the analysis of this event is in favor of the breakout jet model. The coherent brightenings of the IR and CR at $\sim 04:58$ UT may result from the impulsive interchange reconnection near the null point, whereas sub-Alfvénic slipping motion of the western CR in the counterclockwise direction indicates the occurrence of slipping magnetic reconnection.

Acknowledgements. The authors appreciate the referee for valuable suggestions and comments. We also thank K. Yang for discussions. SDO is a mission of NASA's Living With a Star Program. AIA data are courtesy of the NASA/SDO science teams. This work is funded by NSFC grants (No. 11773079, 11790302, 11673035, 11773039, 11903050, 11790304, 11873095), the International Cooperation and Interchange Program (11961131002), the Youth Innovation Promotion Association CAS, the Science and Technology Development Fund of Macau (275/2017/A), the Strategic Priority Research Program on Space Science, CAS (XDA15052200, XDA15320301), and the project supported by the Specialized Research Fund for State Key Laboratories.

References

- Aulanier, G., Golub, L., DeLuca, E. E., et al. 2007, *Science*, 318, 1588
Baumann, G., Haugbølle, T., & Nordlund, Å. 2013, *ApJ*, 771, 93
Brown, J. C. 1971, *Sol. Phys.*, 18, 489
Cargill, P. J., Mariska, J. T., & Antiochos, S. K. 1995, *ApJ*, 439, 1034
Chen, X., Yan, Y., Tan, B., et al. 2019a, *ApJ*, 878, 78
Chen, H., Yang, J., Duan, Y., et al. 2019b, *ApJ*, 879, 74
Demoulin, P., Henoux, J. C., Priest, E. R., & Mandrini, C. H. 1996, *A&A*, 308, 643
Doyle, L., Wyper, P. F., Scullion, E., et al. 2019, *ApJ*, 887, 246
Emslie, A. G., Dennis, B. R., Shih, A. Y., et al. 2012, *ApJ*, 759, 71
Fisher, G. H., Canfield, R. C., & McClymont, A. N. 1985, *ApJ*, 289, 414
Fletcher, L., Dennis, B. R., Hudson, H. S., et al. 2011, *Space Sci. Rev.*, 159, 19
Fletcher, L., Hannah, I. G., Hudson, H. S., et al. 2013, *ApJ*, 771, 104
Hernandez-Perez, A., Thalmann, J. K., Veronig, A. M., et al. 2017, *ApJ*, 847, 124
Hong, J., Yang, J., Chen, H., et al. 2019, *ApJ*, 874, 146
Hou, Y., Li, T., Yang, S., et al. 2019, *ApJ*, 871, 4
Janvier, M., Aulanier, G., Parlat, E., & Démoulin, P. 2013, *A&A*, 555, A77
Janvier, M., Savcheva, A., Parlat, E., et al. 2016, *A&A*, 591, A141
Ji, H., Wang, H., Goode, P. R., Jiang, Y., & Yurchyshyn, V. 2004, *ApJ*, 607, L55
Ji, H., Huang, G., Wang, H., et al. 2006, *ApJ*, 636, L173
Jing, J., Xu, Y., Cao, W., et al. 2016, *Scientific Reports*, 6, 24319
Krucker, S., Hudson, H. S., Jeffrey, N. L. S., et al. 2011, *ApJ*, 739, 96
Lemen, J. R., Title, A. M., Akin, D. J., et al. 2012, *Sol. Phys.*, 275, 17
Masson, S., Parlat, E., Aulanier, G., et al. 2009, *ApJ*, 700, 559
Masson, S., Aulanier, G., Parlat, E., et al. 2012, *Sol. Phys.*, 276, 199
Li, T., & Zhang, J. 2015, *ApJ*, 804, L8
Li, Y., Sun, X., Ding, M. D., Qiu, J., & Priest, E. R. 2017a, *ApJ*, 835, 190
Li, H., Jiang, Y., Yang, J., et al. 2017b, *ApJ*, 836, 235
Li, T., Yang, S., Zhang, Q., Hou, Y., & Zhang, J. 2018, *ApJ*, 859, 122
Li, H., & Yang, J. 2019, *ApJ*, 872, 87
Priest, E. R., & Pontin, D. I. 2009, *Physics of Plasmas*, 16, 122101
Qiu, J., Lee, J., Gary, D. E., & Wang, H. 2002, *ApJ*, 565, 1335
Qiu, J., Wang, H., Cheng, C. Z., & Gary, D. E. 2004, *ApJ*, 604, 900
Qiu, J. 2009, *ApJ*, 692, 1110
Qiu, J., Longcope, D. W., Cassak, P. A., & Priest, E. R. 2017, *ApJ*, 838, 17
Romano, P., Falco, M., Guglielmino, S. L., & Murabito, M. 2017, *ApJ*, 837, 173
Savcheva, A., Parlat, E., McKillop, S., et al. 2016, *ApJ*, 817, 43
Sharykin, I. N., & Kosovichev, A. G. 2014, *ApJ*, 788, L18
Wang, H., & Liu, C. 2012, *ApJ*, 760, 101
Wyper, P. F., Antiochos, S. K., & DeVore, C. R. 2017, *Nature*, 544, 452
Wyper, P. F., DeVore, C. R., & Antiochos, S. K. 2018, *ApJ*, 852, 98
Xu, Z., Yang, K., Guo, Y., et al. 2017, *ApJ*, 851, 30
Yang, S., Zhang, J., & Xiang, Y. 2015, *ApJ*, 798, L11
Yang, S., & Zhang, J. 2018, *ApJ*, 860, L25
Zhang, Q. M., Chen, P. F., Guo, Y., Fang, C., & Ding, M. D. 2012, *ApJ*, 746, 19
Zhang, Q. M., Li, D., Ning, Z. J., et al. 2016a, *ApJ*, 827, 27
Zhang, Q. M., Li, D., & Ning, Z. J. 2016b, *ApJ*, 832, 65
Zhang, Q. M., & Ni, L. 2019, *ApJ*, 870, 113
Zhang, Q. M., Li, D., & Huang, Y. 2019a, *ApJ*, 870, 109
Zhang, Q. M., Cheng, J. X., Feng, L., et al. 2019b, *ApJ*, 883, 124
Zhao, J., Gilchrist, S. A., Aulanier, G., et al. 2016, *ApJ*, 823, 62